Numerical simulation of cone penetration test by using CFD–DEM coupled analysis

Ying Ge[1] · Annan Zhou[1] · Majid Nazem[1] · Yongfeng Deng[2]

Abstract

Precise stratigraphic characterization and assessment of soil parameters are essential for agricultural and geotechnical engineering. The cone penetration test (CPT) has become one of the most extensively used techniques for soil site assessment, because of its reproducibility, robustness, accuracy, and simplicity. The existing DEM (discrete element method) simulations on CPT are only applicable to dry soil, which cannot consider fluid phase (i.e., pore water) and its interaction with the soil particles. The combined DEM and CFD (computational fluid dynamics) approach is developed to model CPT testing on saturated soils in this study. Several sets of CPT simulations at various penetration rates have been performed by using CFD–DEM coupled analysis. The variation of penetration velocity leads to different magnitudes of fluid force, and the variation in fluid force, in turn, affects the CPT measurement of soil's characteristics. Furthermore, the study extends beyond the properties of the soil itself to explore the complex interplay among soil particles, the surrounding fluid environment, and the penetrometer. The cumulative interactions among these elements highlight the intricate nature of CPT and underline the importance of comprehensive computational models in enhancing our understanding of these dynamics.

Keywords Coupled CFD–DEM analysis · CPT · Fluid phase · Mechanical behavior · Penetration velocity · Saturated soil

1 Introduction

The cone penetration test (CPT) is a widely used in-situ testing technique in agricultural and geotechnical engineering that provides essential information on soil profiles and parameters while minimizing interference to the surveyed geology [24]. It is known for its speed, repeatability, reliability, and affordability compared to other field test methods [43]. CPT has been extensively studied through different methodologies, including theoretical analyses [54, 66, 71, 73], experiments [11, 21, 48], and numerical methods [1, 30, 72]. Numerical methods, particularly finite element method (FEM), material point method (MPM), and smoothed particle hydrodynamic (SPH) method, have gained significant attention in CPT studies due to their low cost and excellent efficiency. Early FEM models of CPT used small deformation assumption and simulated a limited number of penetration steps [26, 39]. Then the Arbitrary Lagrangian Eulerian (ALE) and auto-adaptive remeshing technique were utilized to release large displacement FEM modeling of CPT tests [46, 57, 67]. Recent advances in MPM [7, 15] and SPH methods [10] provide alternative methods to enable accurate simulations of large deformations during penetration.

Continuum-based models can provide an approximate representation of the macroscale response of CPT, but they do not explicitly consider the interactions between the soil particles and the penetrator. This limitation becomes particularly critical when analyzing the microscale interactions and mechanics that significantly influence the CPT results. The discrete element method (DEM), first

✉ Annan Zhou
annan.zhou@rmit.edu.au

1 Discipline of Civil and Infrastructure Engineering, School of Engineering, RMIT University, Melbourne, VIC 3001, Australia

2 Institute of Geotechnical Engineering, School of Transportation, Southeast University, Nanjing 210096, Jiangsu, China

developed by Cundall and Strack [18], provides information on the response of granular materials at various spatial scales. DEM enables a detailed examination of particle-level mechanics, offering insights into contact forces, particle displacements, and stress distributions crucial for understanding granular soil behavior during CPT. Many studies have explored the CPT in granular materials by using DEM analyses, to better understand the micro/-macroscale behavior of granular materials and how they interact with the penetrator during penetration process. For example, early work by Huang and Ma [29] used two-dimensional (2D) DEM to simulate deep penetration in sand and demonstrated that the loading history of granular materials significantly influences on both the soil dilatancy and penetration mechanism. By using 2D DEM analyses, Jiang et al. [33] investigated the evolutions of the velocity, deformation, and stress fields, as well as the displacement and stress paths throughout the entire penetration process. Kinloch and O'Sullivan [38] studied the mechanism of failure of the soil granules that interact with the penetrometer and observed a recurring pattern in the rotational orientation of these particles by using 2D DEM methods. As computational power increases, DEM models have transitioned from 2 to 3D and taken more influence factors into consideration. For example, Butlanska et al. [12] replicated CPT tests in a virtual calibration chamber packed with spherical particles and their simulations exhibited quantitative agreement with the tests carried out in laboratory calibration chambers. The influence of soil crushability and irregular particle shape on CPT have been addressed by using DEM [17, 23]. Particularly, in agricultural engineering applications, Kotrocz et al. [40] employed DEM analysis to investigate the effects of the soil model's geometrical changes on variations in the soil penetration resistance. As DEM methods for investigating penetration become more sophisticated, researchers are applying them to more complex but more practical problems. For instance, Khosravi et al. [36] conducted DEM simulations of CPT to investigate the influence of various modeling parameters on CPT responses, particularly tip resistance and friction sleeve shear stress. Their study focused on how interparticle contact parameters, boundary conditions, and void ratio affect these measurements, offering insights into CPT-based soil classification within the framework of soil behavior type (SBT) charts. Sharif et al. [56] used DEM to simulate penetration tests and forecast installation needs by considering the impact of installation pitch and foundation geometry for rotational installed piles in sand. However, it should be noted that these DEM models are all aimed at performing penetration tests in dry soils because DEM that places emphasis on the interaction among discrete elements has difficulty to simulate pore fluid that features continuous flow.

Most of the world's metropolitan areas are located along coastlines and soils in such areas are usually saturated with water in geotechnical engineering and agricultural engineering problems. Thus, the influence of fluid phase (i.e., pore water) in the soils cannot be ignored in many engineering practices, including CPT. For example, unlike in the DEM analysis, saturated soils are widely employed in laboratory CPT tests [27, 41, 47, 52, 55] as well as numerical simulations, such as FEM [5, 35, 45] and MPM [9, 14, 16]. It is worth noting that different penetration rates in saturated soils lead to varying fluid-particle interactions. The penetration resistance and CPT results can be very different because of the influence of pore water in saturated soils to cone penetration [52, 55, 59, 70]. Therefore, as an important tool for studying CPT, DEM is naturally demanded to be extended from dry soils (single-phase porous medium) to saturated soils (two-phase porous medium). Such an extension can be achieved by coupling computational fluid dynamics (CFD) with DEM. The concept of CFD–DEM coupled analysis, first introduced by Tsuji et al. [64], has already been used to address fluid-related geotechnical engineering problems like suffusion, liquefaction and well drilling [2, 31, 42]. This approach provides precise fluid-particle interactions and can capture both micro- and macro-characteristics of both particles and fluids. Therefore, the CFD–DEM approach has great potential to offer new insights to the micromechanical and microhydraulic factors that underly the macroscopic responses of CPT in saturated soil.

The purpose of this study is to investigate CPT tests in saturated soils by developing the coupled CFD–DEM method. The coupling method that enables two-way information exchange between DEM and CFD is validated using the Ergun test and the upward seepage test in a sphere-based column. Several sets of CPT simulations are performed at different penetration rates to explore the behavior of saturated soils in CPT tests, which are also compared with the penetrations in dry soil at the same velocities to illustrate the influence of fluid phase on the CPT process. Furthermore, penetration resistance, change of particle motion, evolution of contact force and mechanical quantities of the fluid phase are analyzed to identify the macro/micro-interaction mechanism among soil particles, pore fluid and penetrator during the penetration process. Finally, some concluding remarks raised from the study are summarized to shed light on the CPT in saturated soils.

2 CFD–DEM coupling approach

The coupling of CFD and DEM in this study is achieved by using the open-source CFD program, OpenFOAM, and a DEM software, PFC3D. This section provides a brief description of the mathematical formulations used to define the physical properties and mechanical principles of the developed CFD–DEM model, as well as the coupling technique. Furthermore, a benchmark analysis (the Ergun test and the upward seepage in a sphere-based column test) is presented to validate the accuracy of the coupling approach.

2.1 Governing equations of the DEM

In the CFD–DEM coupling method, the particle phase is governed by Newton's law of motion. The numerical solution is conducted in the Lagrange frame at a microscale level using DEM. The governing equations of the solid phase are represented by

$$\frac{\partial \vec{u}}{\partial t} = \frac{\vec{f}_{\text{mech}} + \vec{f}_{\text{fluid}}}{m_{\text{P}}} + \vec{g} \tag{1}$$

$$\frac{\partial \vec{\omega}}{\partial t} = \frac{\vec{M}}{I} \tag{2}$$

where $\vec{u}$, t, m_{P}, $\vec{g}$, $\vec{\omega}$, $\vec{M}$ and I represent the particle linear velocity vector, computing time, mass of particles, gravitational acceleration, particle sharp-cornered velocity vector, particle contact moment, and particle moment of inertia, respectively. Besides, $\vec{f}_{\text{mech}}$ is the sum of particle contact force, the non-contact force between particles, and external force, which stands by the total mechanical force acting on the particles. $\vec{f}_{\text{fluid}}$ is the fluid force acting on the particles. The linear parallel bond model, proposed by Potyondy and Cundall [49], is adopted to mimic the interaction between soil particles.

2.2 Governing equations of the CFD

The locally averaged Navier–Stokes equation and the locally averaged continuity equation govern the behavior of the fluid phase. The governing equations are numerically solved within a continuum framework [4, 20]. The fluid phase governing equations are expressed by

$$\frac{\partial (\varepsilon \rho_f)}{\partial t} + \nabla \cdot (\varepsilon \rho_f \vec{v}) = 0 \tag{3}$$

$$\frac{\partial (\varepsilon \rho_f \vec{v})}{\partial t} + \nabla \cdot (\varepsilon \rho_f \vec{v}\vec{v}) = -\varepsilon \nabla p + \varepsilon \nabla \cdot (\mu \nabla \vec{v}) + \varepsilon \rho_f \vec{g} + \vec{f}_b \tag{4}$$

where ε is fluid cell porosity, ρ_f is the liquid density, t is

coupling computing time, $\vec{v}$ is the liquid velocity vector, p is total fluid pressure (excess pore pressure $p' = p - \rho_f gh$), μ is hydrodynamic viscosity, $\vec{g}$ is the acceleration of gravity, $\vec{f}_b$ is the total volume force of per item capacity of the liquid unit imposed by particles at a fluid cell and can be calculated by:

$$\vec{f}_b = \frac{\sum_i^n \vec{f}_d^i}{V_{\text{cell}}} \tag{5}$$

where V_{cell} is fluid cell volume; $\vec{f}_d^i$ is the drag force of the fluid on a single particle in a fluid cell. Note that the total object includes all particles that lie over the liquid unit in the system.

2.3 Interaction forces between fluid and particles

In general, the total fluid-particle interaction force $\vec{f}_{\text{fluid}}$ is composed of two parts: (i) the fluid drag force $\vec{f}_d$ and (ii) the force caused by fluid pressure gradient $\vec{f}_{\nabla p}$. Therefore, the overall fluid-particle interaction force of the fluid acting on the particles can be expressed as follows:

$$\vec{f}_{\text{fluid}} = \vec{f}_d + \vec{f}_{\nabla p} \tag{6}$$

The fluid drag force is the primary catalyst for particle fluidization and the most significant interaction force in the system. According to the circumstances of the fluid unit where the particle is placed, the fluid drag force acting on the particle needs to be described separately. The interaction force between fluid and soil particles continuously operates on the particle center, hence there is no moment acting on these particles. The fluid drag force on the particle cluster is calculated by:

$$\vec{f}_d = \vec{f}_{d0}\varepsilon^{-\chi} \tag{7}$$

where $\vec{f}_{d0}$ indicates the drag force of the fluid on a single particle; ε is the porosity of the fluid cell where the particle is located; $\varepsilon^{-\chi}$ is an empirical correction term used to consider local porosity, which allows the fluid drag force to be applied to systems ranging from high porosity to low porosity and a wide range of particle Reynolds numbers [19, 69]. The fluid drag force on a single spherical particle is calculated:

$$\vec{f}_{d0} = \left(\frac{1}{2} C_d \rho_f \pi r_p^2 |\vec{u} - \vec{v}| (\vec{u} - \vec{v}) \right) \tag{8}$$

where C_d is the drag force coefficient and equal to $(0.63 + \frac{4.8}{\sqrt{\text{Re}_p}})^2$, Re_p is the particle Reynolds number, ρ_f is the fluid density, r_p is the particle radius, $\vec{v}$ is fluid velocity, $\vec{u}$ is particle linear velocity vector. According to literature

[19, 69], the empirical coefficient $\chi = 3.7 - 0.65 \exp\left(-\frac{(1.5 - \lg \mathrm{Re_p})^2}{2}\right)$ and $\mathrm{Re_p} = \frac{2\rho_f r |\vec{u} - \vec{v}|}{\mu}$, where μ is hydrodynamic viscosity. The second part of the interaction force is pressure gradient force $\vec{f}_{\nabla p}$, which is caused by fluid pressure. It is defined by Eq. (9),

$$\vec{f}_{\nabla p} = -V_p \nabla p \tag{9}$$

where V_p is particle volume and ∇p represents the total fluid pressure gradient vector. This pressure gradient force incorporates both the effects of buoyancy due to gravity and the acceleration pressure gradient within the fluid. Under the hydrostatic condition, the equation can be simplified as:

$$\vec{f}_{\mathrm{fluid}} = \vec{f}_d + \vec{f}_{\nabla p} = -\rho_f g V_p \tag{10}$$

where ρ_f is the fluid density, g is the gravitational acceleration, V_p is particle volume.

2.4 Coupling method

The calculation flowchart of the coupling method is shown in Fig. 1:

The CFD–DEM coupling technique is implemented by PFC3D and OpenFOAM. PFC3D runs on the Windows operating system, while OpenFOAM operates on Linux. To achieve coupling between OpenFOAM and PFC3D, the Python programming language is employed to wrap the CFD solver in OpenFOAM as a class-based functional module and make it compatible with the Python

environment in PFC3D. A module ('pyDemFoam') is constructed by Python to incorporate a modified variant of the OpenFOAM icoFoam solver, which is specifically tailored to include porosity and body force terms to account for the presence of particles within the flow. Two distinct versions of icoFoam are provided within this module: The first one ('pyDemIcoFoam') utilizes an explicit formulation for drag as described in the PFC3D manual under the CFD module section; the second one ('pyDemIcoFoamSemiImplicitDrag') employs a semi-implicit drag treatment, to allow for more accurate and stable simulations of fluid–solid interactions.

The fluid-particle-penetrometer coupling encountered in this study can be solved using a coarse-grid method. In this method, it is necessary to numerically solve the governing equations of fluid flow within a series of fluid cells whose sizes are larger than the diameter of the particles in PFC. In PFC3D, the particles and cones of the desired model are generated, and parameters such as particle properties, cone properties, and the cone penetration velocity are specified. Fluid cells are generated in OpenFOAM. Concurrently, within the fluid solver, fluid properties such as density and dynamic viscosity are defined during the discretization of the fluid elements. This process ensures an effective and accurate simulation of the fluid-particle-penetrometer interaction.

To transmit this fluid information mentioned above to PFC, programming operations related to the required functionality must be performed in the PFC data file. Data synchronization and exchange are accomplished through TCP (Transmission Control Protocol) socket
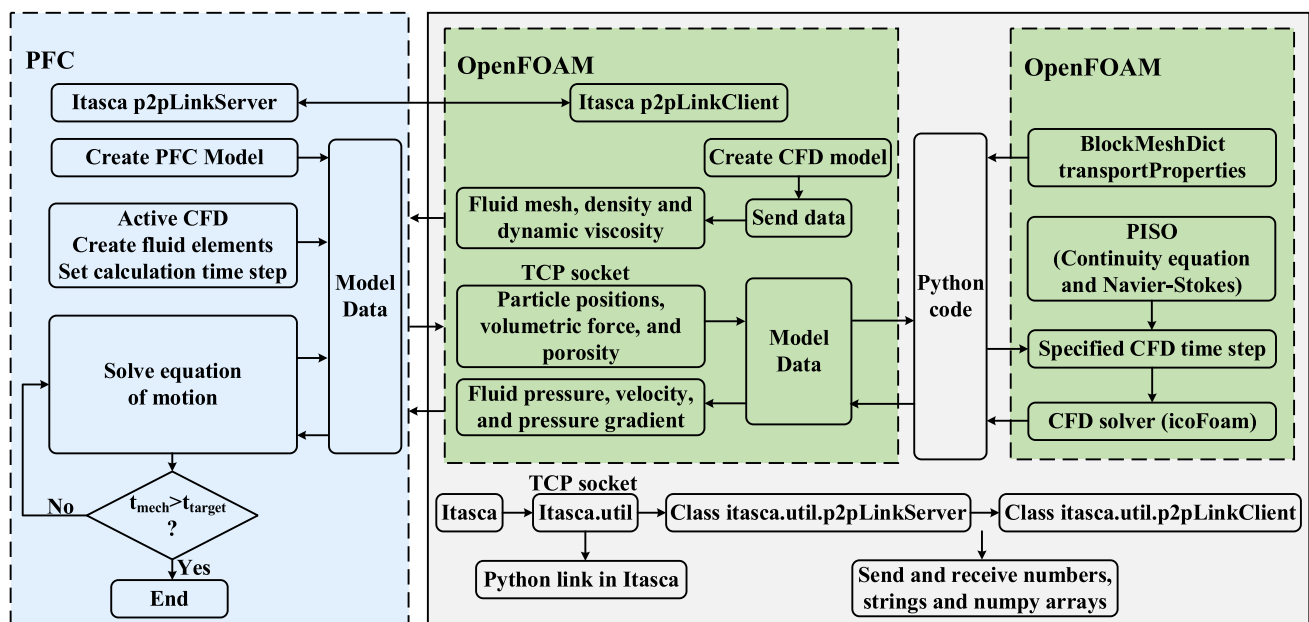

Fig. 1 The calculation flowchart of the coupled CFD–DEM model

communication. The TCP socket class in Python serves as the data exchange interface between OpenFOAM and PFC3D. TCP is a connection-oriented, byte-stream-based transport layer communication protocol, and the socket is the API (Application Programming Interface) for TCP, representing its specific implementation and serving as a necessary API for writing network programs. Within PFC 3D, a Python environment is embedded, which includes the 'itasca' module. The 'itasca.util' sub-module within this module contains two classes, namely 'itasca.util.p2-pLinkServer' and 'itasca.util.p2pLinkClient' which implement all TCP data transmission functionalities. The fluid solver strategically deploys 'itasca.util.p2pLinkClient' to transmit crucial parameters such as fluid mesh, density, and dynamic viscosity to the PFC3D environment. Upon receipt of these fluid parameters, PFC3D activates the CFD module, which consequently reads and utilizes this information to define the domain and generate fluid elements. Adhering to a preordained DEM calculation time step, the first interval of the iterative coupling process is instigated. This stage encompasses the resolution of Newton's equations of motion, followed by an automatic computation of fluid–particle–penetrator interaction forces, subsequently applying them to the particles within PFC. In conjunction, the particle motion characteristics are discerned in accordance with the force–displacement relationship, persisting until the DEM solver time aligns with the designated coupling interval. Post-completion of the DEM solution, the PFC3D software employs the 'itasca.util.p2-pLinkServer' class to relay parameters such as particle positions, volumetric force exerted on each fluid mesh due to the interaction among fluid, particles, and penetrator, porosity, and other physical quantities to the CFD solver. Upon receipt of the particle-associated parameters, the CFD solver harnesses the PISO (Pressure-Implicit with Splitting of Operators) algorithm to solve the discretized fluid pressure–velocity coupling equations, as formulated by the Local Averaging Continuity Equation and Navier–Stokes Equation within the OpenFOAM framework. Following the execution of the CFD calculation in line with the prescribed CFD time step, OpenFOAM updates and re-engages 'itasca.util.p2pLinkClient' to transmit fluid pressure, velocity, and pressure gradient to the DEM solver, thereby culminating one cycle of the coupling calculation. This iterative loop continues to recur until the termination condition is satisfied. In computational simulation, termination condition defines specific criteria for the simulation to stop running. These may include the realization of a specific state, the expiration of a time limit, or the satisfaction of a convergence criterion to ensure that the simulation does not continue indefinitely. The term 't-target' refers to a pre-set time before starting the simulation, the value of which is the time to reach the termination

condition. The 't-mech' refers to the actual time passed during the simulation.

2.5 Benchmarks of the CFD–DEM coupling approach

The benchmarks presented herein serve the purpose of validating the numerical CFD–DEM coupling model. The benchmark problems refer to some typical cases with straightforward analytical solutions that are widely used in the relevant areas. The verification is to check the calculation correctness and efficiency of the numerical model. In this study, the approach is validated by using the Ergun test [22] and the upward seepage flow in a column comprised of individual spheres [58].

2.5.1 Ergun test

The goal of the Ergun test [22] is to simulate the phenomena where water rises to flush the particle bed. The Ergun test equation describing the relationship between the pressure drop Δp and the fluid velocity v_s is shown as:

$$\Delta p = \frac{150\mu L(1-e)^2}{d^2 e^3}v_s + \frac{1.75L\rho(1-e)}{de^3}v_s|v_s| \tag{11}$$

where Δp is the total pressure drop between the fluid inlet and fluid outlet, L is the height of the particle bed, d is the particle diameter, ρ is the fluid density, μ is the viscosity of the fluid, e is the void ratio; and v_s is the fluid velocity.

In this study, the Ergun test is reproduced in several steps. (1) Establish the DEM model: This size of cube model is 31.2 mm × 31.2 mm × 15.6 mm. This sample has a void ratio of 0.45 with particles that range in size from 0.9 to 1.1 mm. (2) Construct the CFD model: The CFD model has a bigger size than the DEM model, which is 32 mm × 32 mm × 100 mm. (3) Start the coupling calculation: The fluid mesh at the bottom boundary was prescribed with a superficial velocity. As fluid moves through the granular cube from bottom to top, the pressure drop at various speeds is being tracked. The CFD–DEM model is displayed in Fig. 2a, and the parameters are shown in Table 1.

In Fig. 2b, the outcome of the CFD–DEM coupling simulation is compared with the result of the analytical solution. When comparing the simulated outcomes with the analytical resolution, it can be found that there is a good match between the total pressure drop curve and the Ergun equation before it reaches a critical value. When the superficial velocity reaches the minimum fluidization velocity, the granular packing will fluidize and result in a constant pressure drop despite an increasing fluid velocity [51], which cannot be reflected by the analytical solution. The satisfactory level of alignment between our forecasted
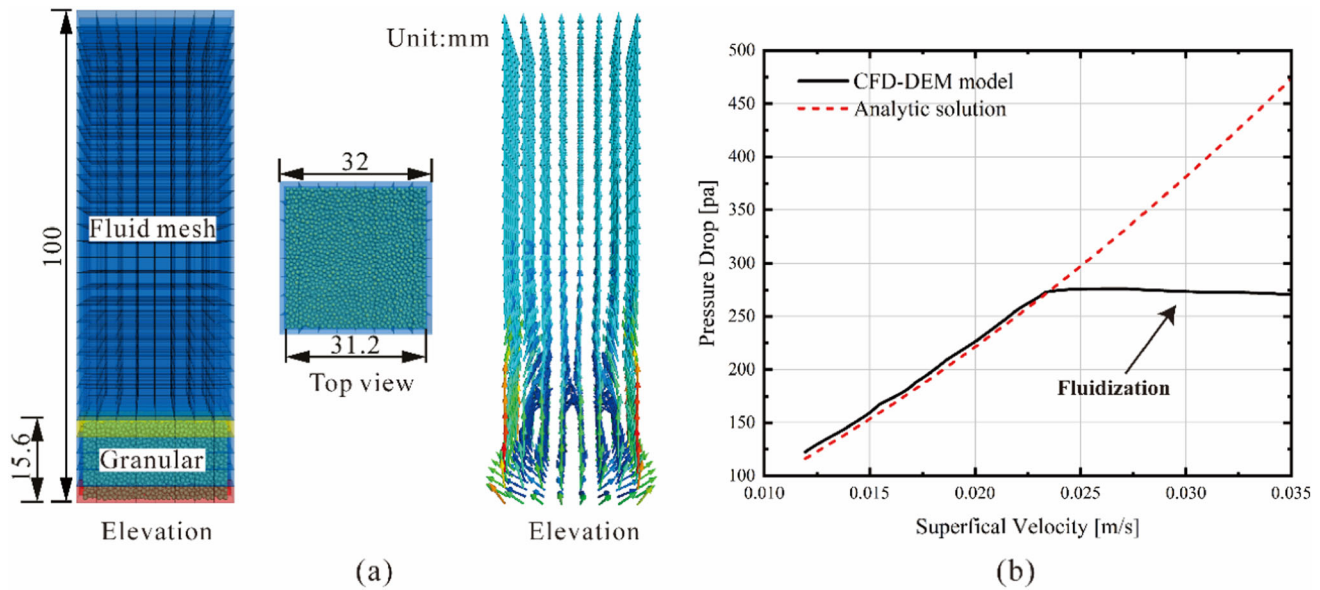
Fig. 2 Modeling the Ergun test using CFD–DEM. **a** The CFD–DEM model; **b** the result of the Ergun test compared with CFD–DEM coupling

Table 1 The parameters of Ergun test

Parameters	Value	Unit
Model shape		
Granular bed height	15.6	mm
Equivalent spherical diameter	1.0	mm
Void fraction	0.45	–
Column width	31.2	mm
Acceleration of gravity	9.81	m/s^2
Solid phase (PFC3D)		
Particle radius	0.45 $\sim$ 0.55	mm
Particle density	2500	kg/m^3
Friction coefficient	0.6	–
Normal stiffness	1e6	N·m^{-1}
Shear stiffness	1e6	N·m^{-1}
DEM timestep	5e-5	s
Fluid phase (OpenFOAM)		
Mesh scale	$32 \times 32 \times 100$	mm
Cell size	$4 \times 4 \times 3.33$	mm
Fluid density	1000	kg/m^3
Dynamic viscosity	1e-3	N·s/m^2
CFD timestep	5e-5	s

and computed results before fluidization corroborates the efficacy of the method employed. This finding implies that the coupled CFD–DEM method, developed in this research, exhibits a commendable proficiency in encapsulating the complex interplay between fluid and multiparticle systems.

2.5.2 Upward seepage flow in a column comprised of individual spheres

The manifestation of the suffusion phenomenon can be discerned through the simulation of seepage flow within packed spheres. The exploration of upward seepage flow within a singular column of spheres provides a streamlined, yet robust model for gauging the fluid forces imposed on larger particles amidst suffusion. Suzuki et al. [58] developed an analytical solution for the settlement of the uppermost spheres in the absence of seepage flow, which is presented as follows:

$$\delta = \frac{N(N+1)}{2k_n} \frac{4\pi}{3} \left(\frac{d}{2}\right)^3 (\rho_\mathrm{p} - \rho_\mathrm{f})g \tag{12}$$

where N represents the number of particles, k_n denotes the spring constant, d represents the diameter of each individual particle, and ρ_f and ρ_p represent the densities of the fluid and particles, respectively. Following the introduction of upward seepage flow with a velocity of 0.005 m/s, the displacement of the uppermost spheres in the column can be described using the following analytical solution [58]:

$$S_t = \frac{u* H^2}{C_v 2} \left(1 - \frac{32}{\pi^3} \sum_{i=0}^{\infty} \frac{(-1)^i}{(2i+1)^3} e^{-T_v(2i+1)^2 \pi^2/4} \right) \tag{13}$$

$$C_v = \frac{k}{m_v \rho_\mathrm{f} g} \tag{14}$$

$$T_v = \frac{C_v t}{H^2} \tag{15}$$

where $u*$ represents the input flow velocity, T_v denotes the time factor, C_v is the coefficient of consolidation, k

represents the coefficient of permeability, m_v is the coefficient of volume compressibility, and H corresponds to the height of the column. The coefficient of volume compressibility (m_v) can be directly determined from the highly idealized model, whereas the coefficient of permeability (k) is derived from experimental findings, as described by Ergun [22] in the following manner:

$$k = \frac{u*}{i} = \frac{\rho_f g}{\frac{1-n}{dn^3} \left\{ 150 \frac{(1-n)}{d} + 1.75 \rho_f u* \right\}} \tag{16}$$

where n is porosity.

The process of modeling the upward seepage for single-column soil particle clusters using CFD–DEM is outlined as follows. The initial phase consists of consolidating the single-column clusters of soil particles, submerged in quiescent water. After the consolidation process is completed, upward percolation is simulated by applying an upward scouring water flow at the bottom of the particle cluster. For the numerical calculation, a cylindrical soil particle cluster consisting of 100 spherical particles of equal size, each having a diameter of 0.001 m and a density of 2650.0 kg/m³, is considered. The soil particle cluster is assumed to be in a saturated state within a water tank with dimensions of 0.001 m × 0.001 m × 0.1 m (length, width, and height, respectively). The fluid in the tank has a density of 1000.0 kg/m³ and a dynamic viscosity of 1.004×10^{-3} Pa·s. The fluid is assumed to be at rest. The entire sink area's flow field is discretized into fluid cells with a height of 0.002 m. In the calculation, the linear contact model utilizes the normal spring model based on Hooke's law, with a normal stiffness of 100.0 N/m. Figure 3a illustrates the numerical model. The geometric configuration and parameters utilized in the CFD–DEM simulation are adopted from the work of Suzuki et al. [58].

Figure 3b illustrates the simulated and analytical solutions for the settlement of the top particles under static water conditions. During this stage, the particle cluster experiences only the effects of gravity and buoyancy. The analytical solution, derived from eq. (12), yields a value of 0.4278×10^{-3} m, while the simulated value is 0.4256×10^{-3} m, resulting in a relative error of 0.51%. Figure 3c presents a comparison between the simulated and analytical displacements of the uppermost particle following the introduction of upward seepage flow at a velocity of 0.005 m/s. The relative error between the analytical solution and the simulated value for the final displacement of the top particle's upward movement is 1.14%. Nevertheless, the notable agreement observed between the predicted and calculated outcomes implies that the coupled CFD–DEM method demonstrates exceptional performance in capturing the interactions between fluid and multiple particles.

3 Model setup and testing procedures

3.1 Model setup and parameter selection

An in-situ testing for penetration resistance was carried out at Gödöllo's experimental farm, by utilizing a standard Eijkelkamp penetrologger (Eijkelkamp, Netherlands) in the track of a GAZ-69 (69A) kind of vehicle [44]. This field experiment was replicated in this study using the DEM approach. The model in Fig. 4 with rectangular cross sections was used to perform the DEM simulations of soil penetration. The DEM model size is $120 \times 120 \times 300$mm. In the rectangular-shaped soil body, a large number of particles (15,244) were produced and fell to the bottom due to gravity. No confining pressure was exerted against the walls in this study. Figure 4 also shows the cone penetrometer's dimensions used in the simulation, which are identical to those of the Eijkelkamp penetrologger. The linear parallel bond model in PFC3D was applied to simulate the interaction between soil particles. The linear part was responsible for simulating the friction between the particles, and the parallel bond part for modeling the cohesive behavior of the soil. Simulations were run with manually altered contact qualities to examine how the different factors (particle stiffness and parallel bond strengths and stiffness) affected the penetration resistance. The estimated soil penetration resistances were compared to the measured values, to ensure the contact parameters were carefully determined to provide predicted soil resistance that were comparable to those observed in situ. The Pearson correlation coefficient (r) between the simulated result and the in-situ outcome is used to examine the correctness of the simulation. This coefficient is a widely used measure of the strength and direction of a linear relationship between two variables. A higher value of r indicates a stronger linear relationship between the two variables. It is defined as the covariance of the two variables divided by the product of their standard deviations, and is calculated as follows:

$$r = \frac{n(\sum xy) - (\sum x)(\sum y)}{\sqrt{\left[n \sum x^2 - (\sum x)^2 \right] \left[n \sum y^2 - (\sum y)^2 \right]}} \tag{17}$$

where n is the number of depths where the soil resistance values were obtained (in this case, $n = 28$), x is the soil resistance from the DEM simulation in MPa, y is the measured soil resistance from the in-situ tests in MPa.

Our simulation results are presented with a high r value of 0.87 in Fig. 5, which is higher than the previous simulation ($r = 0.84$) available in the literature [40] for dry conditions only. This suggests that the chosen parameters (see Table 2) are well enough to calculate the soil
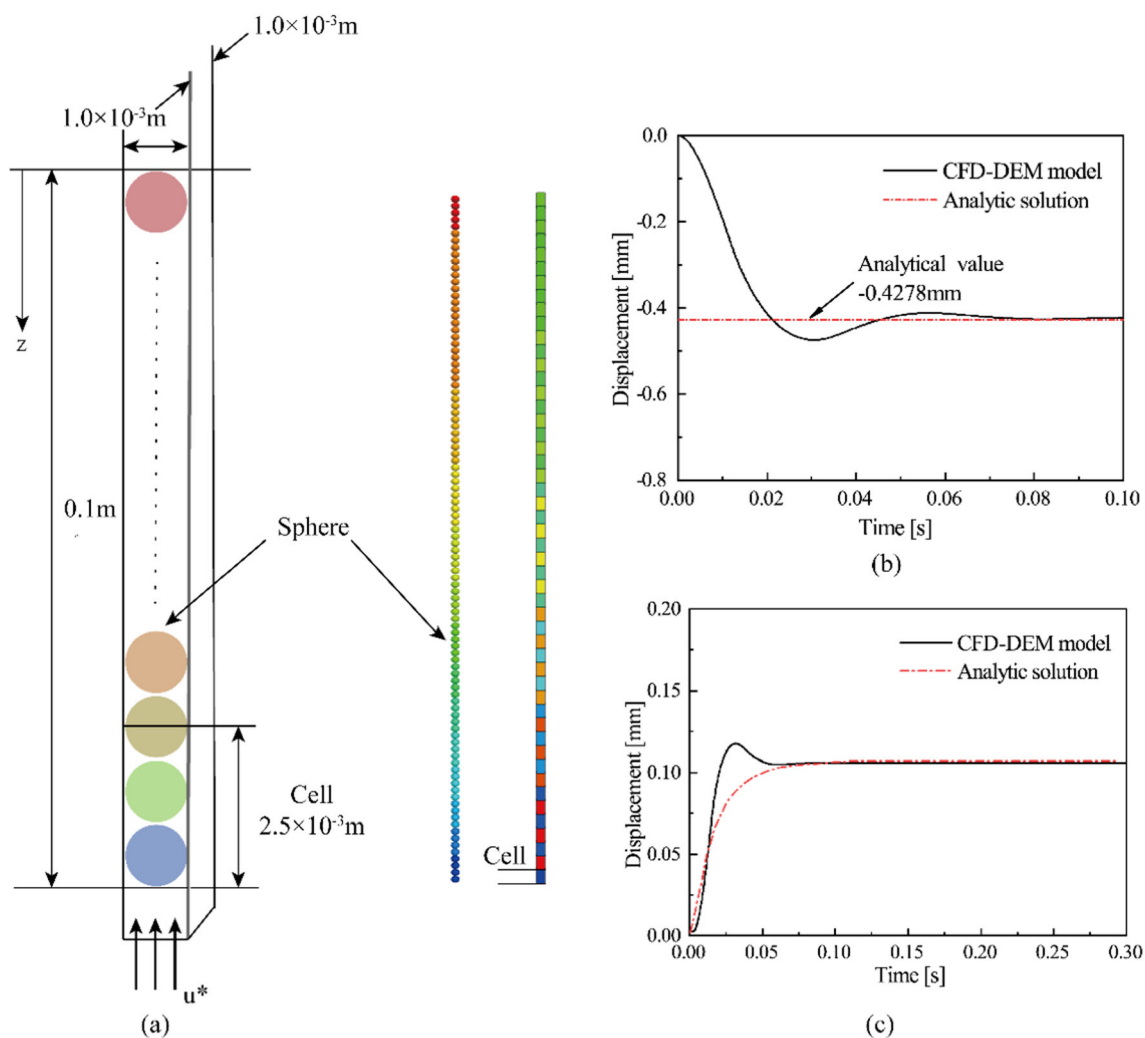
Fig. 3 Modeling upward seepage flow in a column comprised of individual spheres using CFD–DEM. **a** Numerical model schematic; **b** comparison of simulated values and analytical solutions of top particle settlement displacement at hydrostatic time; **c** comparison of simulated values and analytical solutions of top particle displacement during upward seepage

resistance in comparison to the in-situ experiment. Following Kotrocz et al. [40], ground can be separated into two layers (top layer and bottom layer) in terms of normal and shear strength (see Table 2), to represent the actual soil strength observed in the field, where the shallow layer is subjected to weaker normal stresses than the deeper layer. The lower normal and shear strengths of parallel bonds in the top layer (0–0.08 m depth) are set to 1/5 of these values for the bottom layer (0.08–0.3 m).

To consider the behavior of pore fluid during penetration and its influence on the penetrator, the CFD is coupled to the DEM analysis. The CFD domain is $120 \times 120 \times 300$mm which should cover the DEM model (see Fig. 4). The inlet and outlet boundary conditions are free drainage interfaces during the whole process of simulation. The parameters of the fluid phase are selected from

the literature [42, 74]. These parameters are also shown in Table 2.

3.2 Test program for cone penetration tests

It is well known that the CPT tests are frequently employed, primarily for the purposes of classifying soil layers and obtaining indications of each soil layer's engineering qualities. It is acknowledged that the end resistance of CPT varies with penetration velocity [60]. The influence of different penetration velocities on CPTs is considered in addition to saturation states in this study.

The CFD–DEM coupled simulations are launched by the following procedures. (1) Stage 1: Sample preparation. Particles are generated according to the given particle radius and initial void ratio. The cone penetrometer consists of a wall assembly, which is placed on top of the soil
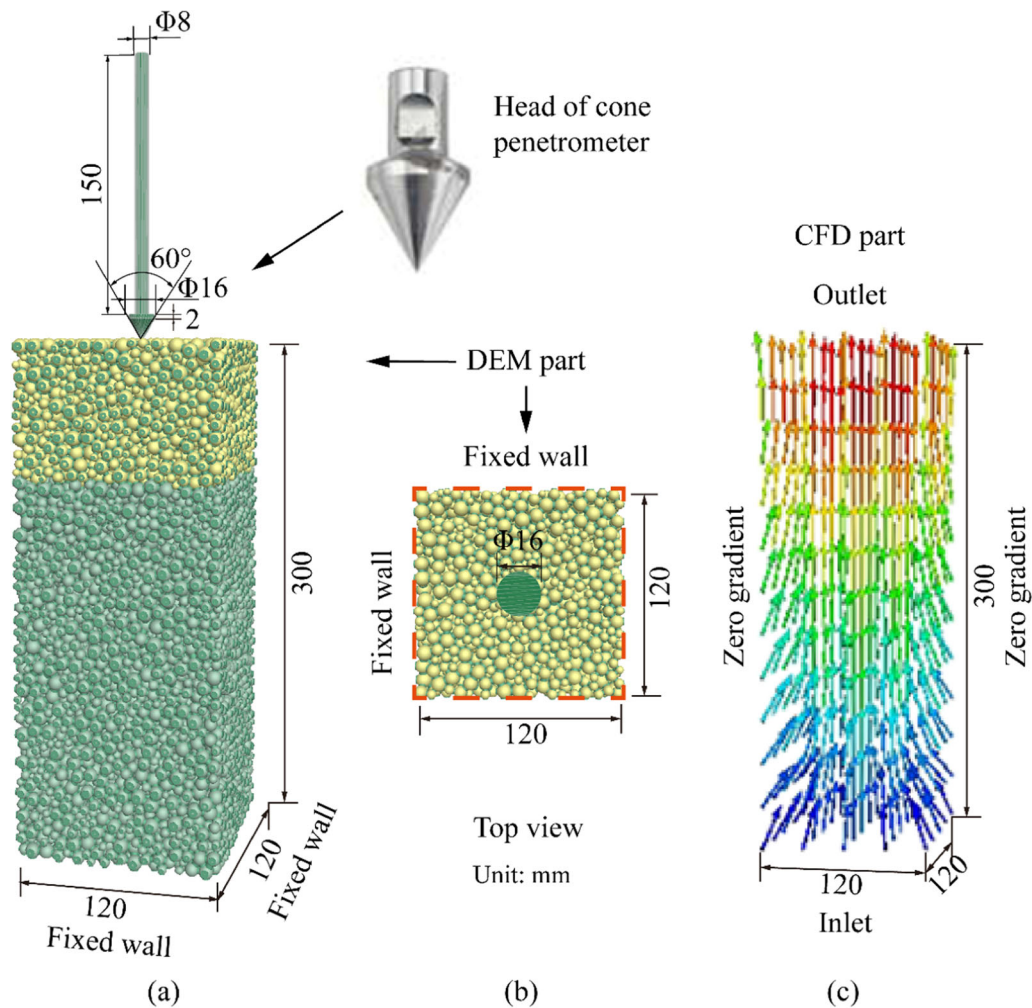
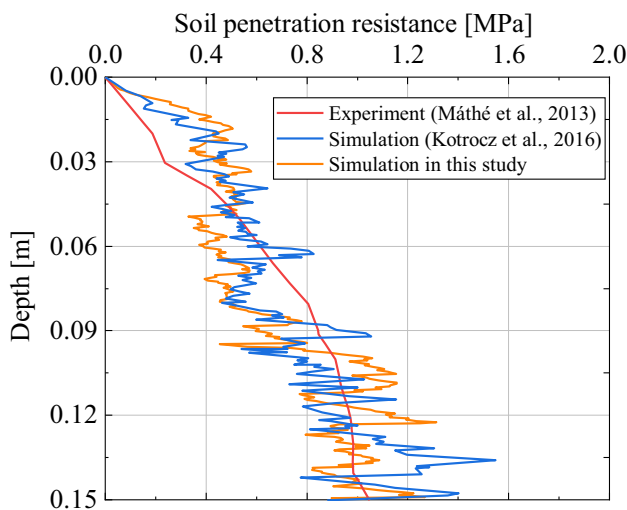**Fig. 4** The CFD–DEM model for cone penetrometer

Fig. 5 Variation in the discrete element method (DEM) simulation of the penetration test

surface. (2) Stage 2: Standing water environment. In this stage, the coupling calculation is switched on, but the cone penetrometer does not commence. The sample is under a standing water environment and the fluid boundary is free. This stage lasts for 0.05 s to achieve hydrostatic equilibrium in the particle–fluid system. (3) Stage 3: Coupling calculation. The cone penetrometer starts to move downwards throughout the soil body to a depth of 0.15 m with a constant velocity in this stage. The water environment is consistent with the previous period. In this stage, the focal point is the penetration rate and the drainage condition. Three different penetration velocities are considered, including 5 mm/s [61], 20 mm/s [50, 53], 100 mm/s [34], and 200 mm/s [3]. Herein, 20 mm/s is the standard penetration rate, at which sand soil is regarded to be fully drained.

Table 2 Parameters adopted for penetration tests

Parameter	Value	Unit
Penetrometer		
Normal stiffness	1e10	N·m^{-1}
Shear stiffness	1e10	N·m^{-1}
Particles		
Particle number	15244	–
Particle density	2810	kg/m^3
Friction coefficient (ball–ball)	0.60	–
Friction coefficient (ball–penetrometer)	0.50	–
Normal stiffness	1e6	N·m^{-1}
Shear stiffness	1e6	N·m^{-1}
Radius range	2.0–4.5	mm
Radius (2.0–2.5 mm)	6.7	%
Radius (2.5–3.0 mm)	11.4	%
Radius (3.0–3.5 mm)	17.9	%
Radius (3.5–4.0 mm)	26.3	%
Radius (4.0–4.5 mm)	37.7	%
Porosity	0.42	–
Contact		
Parallel bond normal strength (top layer)	1e5	Pa
Parallel bond shear strength (top layer)	1e5	Pa
Parallel bond normal strength (bottom layer)	3e5	Pa
Parallel bond shear strength (bottom layer)	3e5	Pa
Fluid		
Cell size	24 × 24 × 25	mm^3
Fluid density	1000	kg/m^3
Dynamic viscosity	1.0e-3	N·s/m^2
Global setting		
Coupling time step	1e-4	s
Gravitational acceleration	9.8	m/s^2

4 Numerical results and discussion

4.1 Macroscopic behavior

This study aims to understand the effect of penetration velocity on cone resistance in saturated sand (dry sand is also employed as benchmark). For this purpose, saturated sand samples were prepared, and cone penetration tests were carried out at a wide range of penetration rates. The calculated soil penetration resistance was shown as a function of the vertical displacement of the cone (see Fig. 6). Here the penetration resistance is the vertical force exerted on the cone by the water and the particles together. At the same time, the number of elements in contact with the tip of the cone was also calculated to check whether there were enough balls around the tip and correct soil resistance change.
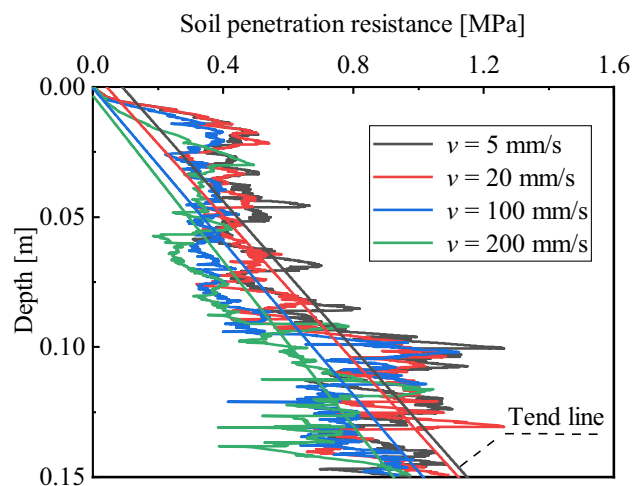
Fig. 6 The effect of penetration rate on penetration resistance in saturated sand

Similar to previous studies [25, 62], the simulated cone penetration resistance fluctuates greatly, with greater fluctuation observed with increased depth [25]. The reason for this result could be attributed to the large diameter of the particles [62]. To observe more clearly the trends of cone tip resistance at different rates, a statistical analysis method was used to re-analyze the original cone tip resistance curves (see Fig. 7a and b), where the depth was divided into five sections and the mean value of the penetration resistance was calculated for each section. As shown in Fig. 7a (saturated sand) and 7b (dry sand), the average value of penetration resistance for each section increases with depth for various penetration velocities. This result is in accord to the field observation because the top layer is subjected to lower normal stresses than deeper layers in general. The resistance of saturated sand decreases tangibly with increasing penetration velocity; however, the velocity has minimal impact on the dry sample (shown in Fig. 7b for comparison purposes). This result is in agreement with the in-situ finding of Jezequel [32]. The explanation for this finding will be discussed in detail in the following sections.

4.2 Micromechanical analysis

The DEM numerical simulation enables us to study the CPT test at the particle scale. The evolution of the displacement field, the velocity field, and the contact force can be determined and visualized, while these results are difficult to obtain through experiments and field tests. The microscopic study of the particle system can help us to understand the movement trend of particles.

4.2.1 Displacement and velocity field

The variation of soil particle displacement and velocity field at different velocities is similar. Therefore, the case of 20 mm/s penetration rate is used to show this evolution in saturated soil during the penetration process (see Fig. 8). According to the previous numerical simulations on dry soil, the maximum displacement of soil particles occurs near the cone penetrometer [25, 40, 62]. The progression of the displacement field of saturated sand, shown in Fig. 8, displays the similar characteristics of the movement of particles in dry soil. Tanaka et al. [62] explained that the soil grains near the penetrometer shaft moved with the downward movement of the penetrometer because of the high friction coefficient between the soil particles and the CPT penetrometer. The displacement distribution of soil was symmetrical, and the movements of soil particles at the cone tip were distributed in a circular shape and decreased along the radius (see Fig. 8).

Figure 9 demonstrates the evolution of the particle velocity at different stages of the CPT with a penetration velocity of 20 mm/s. In common with the previous study [13], the maximum velocity field appeared next to the cone tip of the penetrometer. The pattern of the velocity field takes different shapes for different penetration stages. In the progress of shallow penetration (see Fig. 9a), the particles near the cone tip move mainly sideward and upward, which is following Terzaghi's theory [63]. In contrast to this view, Biarez et al. [8] and Hu [28] suggest that during penetration, half of the particles near the penetrometer's shoulder move upward and sideward, while the other half move downward and sideward. Figure 9b presents a
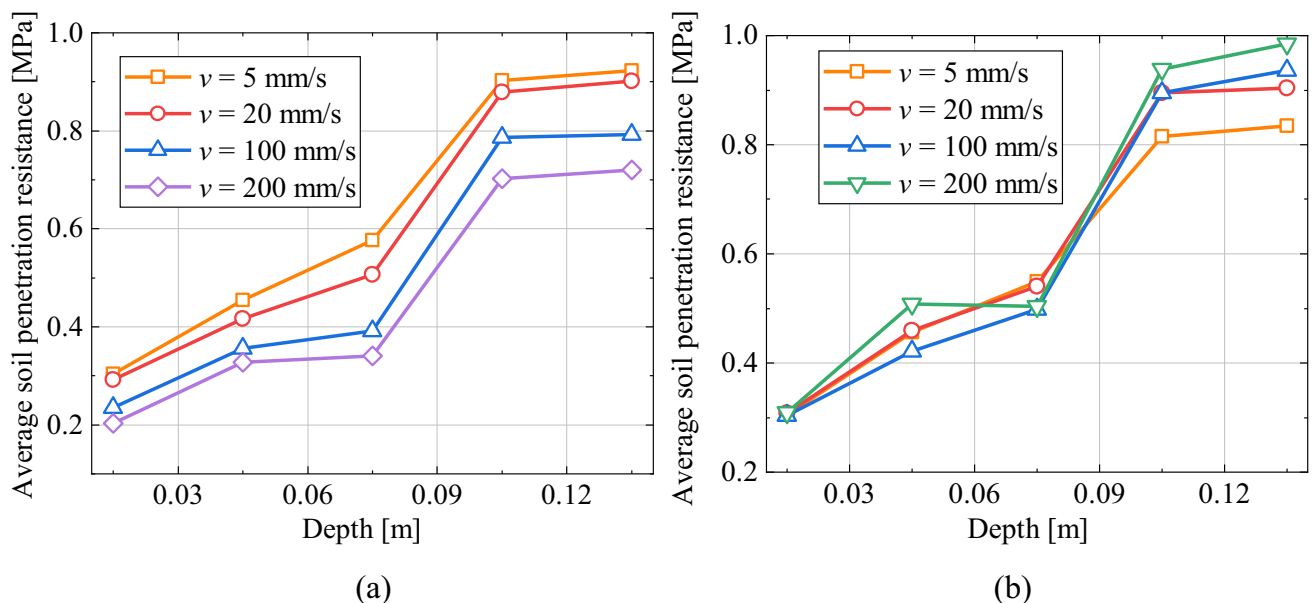

Fig. 7 Average penetration resistance with depth under various penetration velocities. **a** saturated soil; **b** dry soil
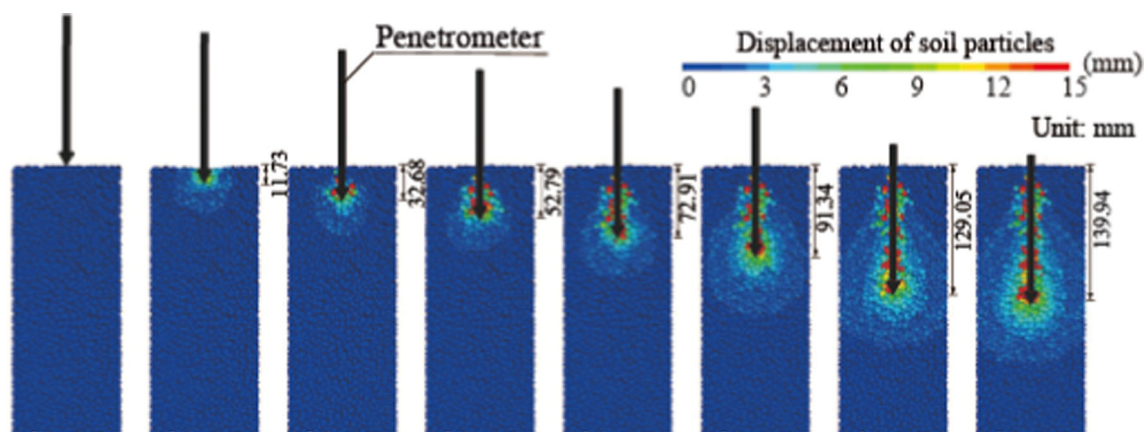
Fig. 8 Displacement distribution of soil particles at a penetration rate of 20 mm/s
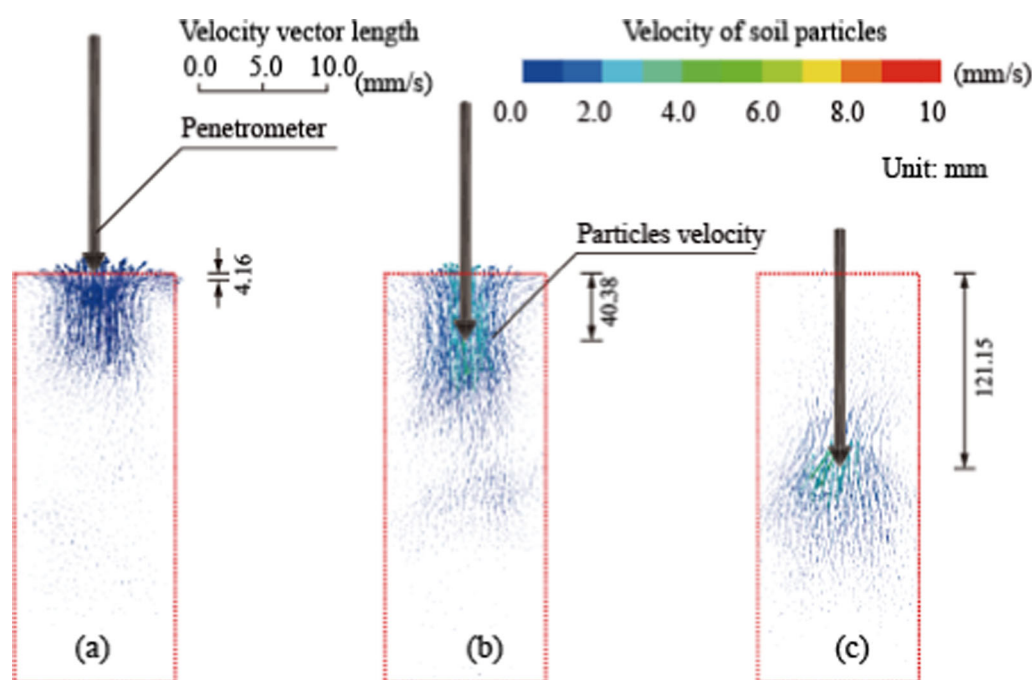

Fig. 9 Velocity distribution of soil particles at a penetration rate of 20 mm/s. **a** shallow process; **b** medium process; **c** deep process

similar observation to their understanding, indicating that the theory proposed by Biarez et al. [8] and Hu [28] is more suitable for deeper penetration. With further penetration, the particles near the tip of the cone move more downward than upward (see Fig. 9c). This phenomenon is consistent with the penetration breaking mechanism proposed by Berezantzev [6] and Vesic [65].

4.2.2 Contact force

Interparticle contact is widely considered to be one of the important factors determining the mechanical properties of particles. As shown in Fig. 10, spatial directions of contacts can be represented by a function of two angles θ and

φ in the three-dimensional (3D) coordinates [68]. The orientations of the contact can be defined in terms of an angular distribution function $E(\theta, \varphi)$, where the angular interval $(d\theta, d\varphi)$ represents the contact distribution portion. The load considered in this study is symmetric about the Z-axis and thus the effect of θ can be eliminated. Therefore, the angular distribution equation can be simplified as $\overline{E}(\varphi) = \frac{\int_0^{2\pi} E(\theta,\varphi)d\theta}{\int_0^{2\pi} d\theta}$. The function $\overline{E}(\varphi)$ with respect to φ and $\varphi + \pi$ is physically equivalent and it thus can always be expressed in terms of a Fourier series containing even components. Its approximate form based on the second Fourier component can be expressed as follows:
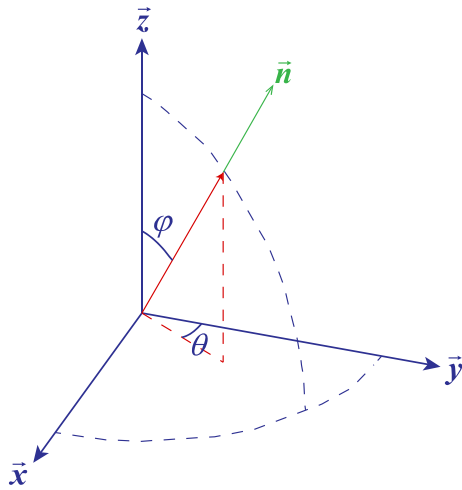
Fig. 10 Three-dimensional framework

$$\overline{E}(\varphi) = \frac{1}{2\pi}[1 + \alpha\cos 2(\varphi - \beta)] \tag{18}$$

where α is the parameter indicating the degree of anisotropy (α^n for normal contact force, α^s for shear contact force) and β is the parameter on the anisotropic direction (β^n for normal contact force and β^s for shear contact force). When $\alpha = 0$, the distribution of contacts is considered to be isotropic and $\overline{E}(\varphi) = 1/2\pi$ to ensure that $\int_0^{2\pi} \overline{E}(\varphi)d\varphi = 1$. specifically, α and β can be indicated as:

$$\alpha = 2\sqrt{\left[\int_0^{2\pi}\overline{E}(\varphi)\cos 2\varphi d\varphi\right]^2 + \left[\int_0^{2\pi}\overline{E}(\varphi)\sin 2\varphi d\varphi\right]^2} \tag{19}$$

$$\beta = \frac{1}{2}\arctan\frac{\int_0^{2\pi}\overline{E}(\varphi)\sin 2\varphi d\varphi}{\int_0^{2\pi}\overline{E}(\varphi)\cos 2\varphi d\varphi} \tag{20}$$

Figure 11 presents the normal and tangential contact forces information of the cases under various penetration velocities in both dry and saturated states. The first two rows show the distribution of normal contact forces for the initial and final states of the saturated and dry soil samples at 4 different penetration velocities. The bottom two rows show the distribution of tangential contact forces for the initial and final states of the saturated and dry soil samples at 4 different penetration velocities. The height and the color of each column in the spherical coordinate system varies with the statistical contact intensity, i.e., a higher column means more concentrated distribution, and warmer color shows greater contact force. In the initial state, the contact distribution of dry and saturated soils is similar, showing peanut shaped. This is because of gravity, and the contact is mainly distributed in the vertical direction. As the penetration progressed, the shape of the contact distribution of each case developed to a spherical shape to

varying degrees at the final state. This represented a decrease in the degree of anisotropy under the perturbation of the penetrators. Comparing the dry soil cases at different velocities, the coefficients did not differ significantly, indicating that the penetration velocity did not affect the degree of anisotropy of the final state of the penetrated soil sample. However, for saturated soils, it is noticeable that the anisotropy coefficient increases as the velocity becomes larger, suggesting that in saturated soils, the greater the velocity, the greater the degree of anisotropy in the final soil pattern.

Figure 12 shows the values of normal contact forces for saturated and dry soils using different penetration velocities at the final state. Comparing to dry soil, the overall normal contact forces of saturated soil are smaller than that of dry soil. Particularly at high velocity (such as 100 mm/s and 200 mm/s), the normal contact force of saturated soil becomes significantly smaller. When penetration velocity increases, the normal contact force for both dry and saturated soils decreases. Compared to dry soils, the velocity effect on saturated soil's contact force is significant. The sharp reduction of contact force with increase of penetration velocity explains the penetration resistance decrease observed in Fig. 7a.

4.3 Microhydraulic analysis

In the simulation of this study, the fluid is set to a still water environment and at a free boundary. It means that under the action of no external load, the water flow remains stagnant or has little fluidity, but once there is an interference of an external load, the water can flow out of the boundary. In the process of cone inserting, the fluid starts to flow due to the dynamic head difference caused by the increase in pressure. Compared with other existing numerical simulation methods for simulating the cone penetration test on saturated soil, the CFD module of the CFD–DEM method can draw the fluid force nephogram, the velocity vector diagram, etc., so that the flow process during penetration can be observed intuitively.

4.3.1 Fluid force

The fluid force variations including pressure gradient force and fluid drag force are influenced by different penetration velocities, as illustrated in Fig. 13a and b, respectively. At the same scale, an increase in velocity leads to greater pressure gradient force, as well as a larger diffusion area, generated as a result of the cone insertion. They all exhibit the same phenomenon. Pressure gradient forces are observed in the part of the soil that cone tip has already passed and near the cone tip. Pressure gradient forces
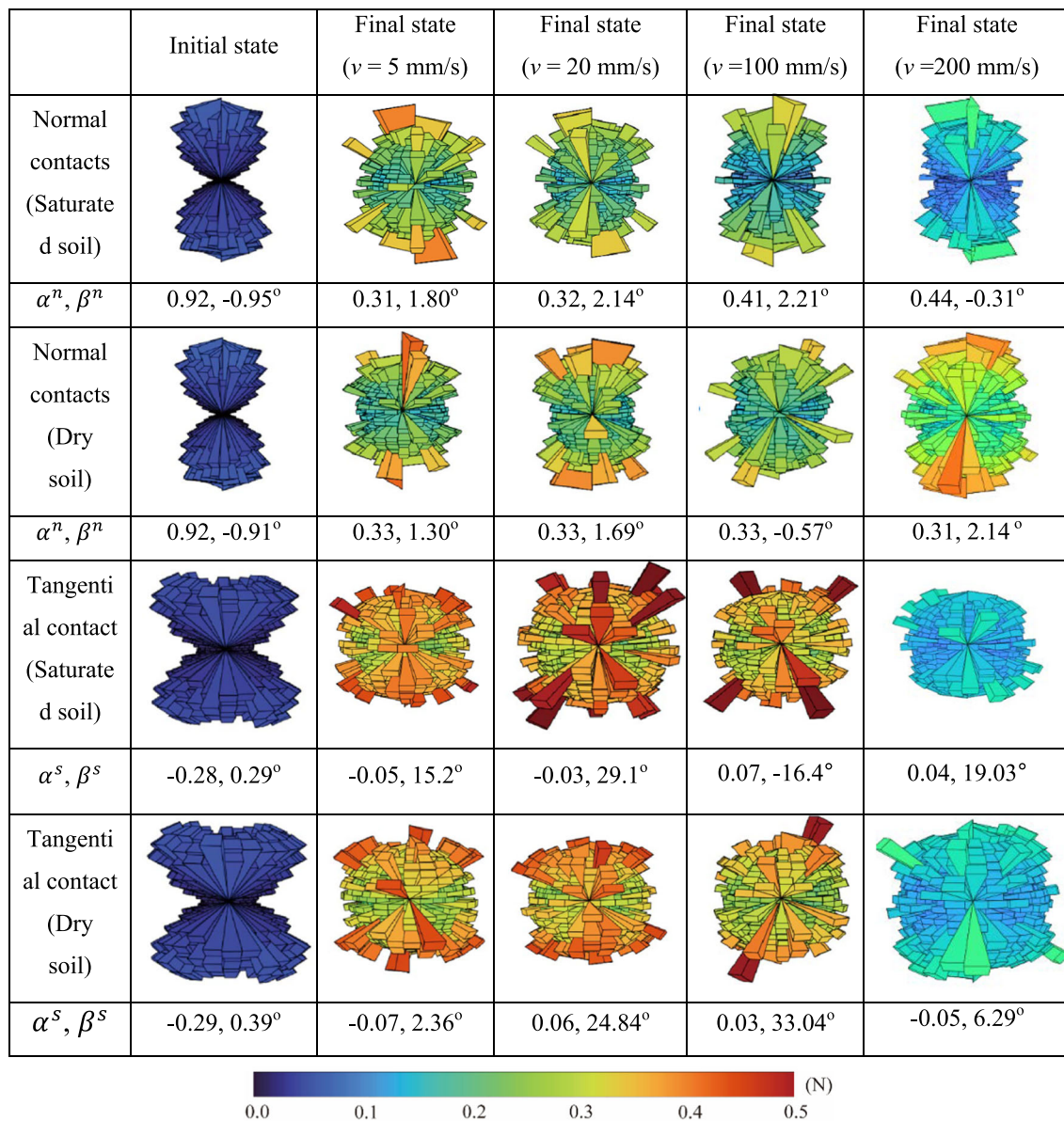
	Initial state	Final state (v = 5 mm/s)	Final state (v = 20 mm/s)	Final state (v =100 mm/s)	Final state (v =200 mm/s)
Normal contacts (Saturated soil)					
α^n, β^n	0.92, -0.95°	0.31, 1.80°	0.32, 2.14°	0.41, 2.21°	0.44, -0.31°
Normal contacts (Dry soil)					
α^n, β^n	0.92, -0.91°	0.33, 1.30°	0.33, 1.69°	0.33, -0.57°	0.31, 2.14°
Tangential contact (Saturated soil)					
α^s, β^s	-0.28, 0.29°	-0.05, 15.2°	-0.03, 29.1°	0.07, -16.4°	0.04, 19.03°
Tangential contact (Dry soil)					
α^s, β^s	-0.29, 0.39°	-0.07, 2.36°	0.06, 24.84°	0.03, 33.04°	-0.05, 6.29°

(N)
0.0   0.1   0.2   0.3   0.4   0.5

Fig. 11 Orientations of normal and tangential contacts for saturated and dry soils under various penetration velocities

become more distinct in both magnitude and diffusion area when penetration velocity increases.

As the penetration velocity increases, the intensity and range of drag forces around the cone are markedly heightened. This phenomenon may stem from the fact that the cone provides a greater kinetic potential energy to the water as it passes through the soil at a higher velocity, resulting in a rapid flow of water. This rapid fluid movement significantly increases the drag force of the fluid on the soil particles, pushing particles away from the path of penetration. Comparing the values of drag and pressure gradient force, the magnitude of drag force is significantly greater than that of pressure gradient force. The significant increase in the fluid drag force, rather than pressure

gradient force (related to total pore water pressure), leads to significant reduction of normal contact force (see Fig. 12) and cone penetration resistance (see Fig. 7a) for saturated soils owing to velocity increase. Thus, the drag force responds to changes in penetration velocity more significantly to the soil-fluid system than the pressure gradient force, which emphasizes the dominant influence of drag force under dynamic conditions.

Figure 14 shows a detailed analysis of the drag force distribution along the x-axis at varying depths and penetration velocities. The graph is divided into three panels, each representing different penetration depths (37.5 mm, 75 mm, and 150 mm), with drag force measurements plotted against x-axis. Across these panels, the drag force
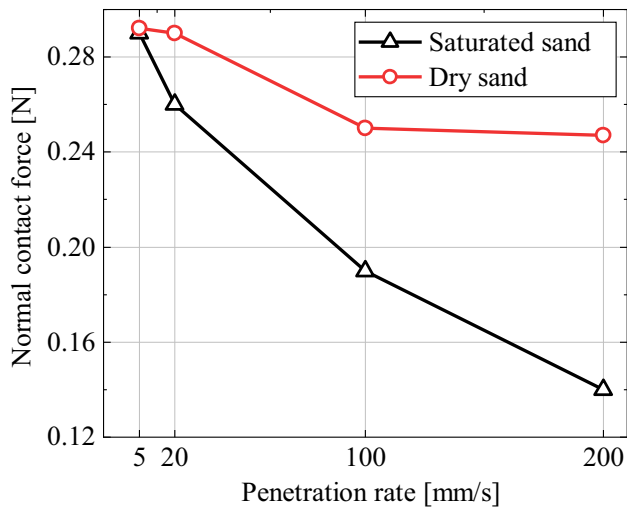
Fig. 12 Normal contact force of dry and saturated sand after penetration at different penetration rates

profiles for different velocities are illustrated using distinct color for clarity. Notably, at higher velocity, there is a significant peak in drag force observed particularly around the middle of the *x*-axis (i.e. where the penetrometer is located), indicating a localized and intense increase in drag force at higher velocities around penetrometer. This effect becomes more pronounced with increased penetration depth, suggesting that both the depth and velocity of penetration substantially influence the magnitude and distribution of drag forces.

4.3.2 Flow rate and direction

Figure 15 presents the velocity evolution characteristics of the flow field during the penetration process with the standard penetration velocity of 20 mm/s as an example (the pattern is similar for other velocities). The flow field is relatively stationary before penetration. With the penetration of the cone, the flow field is gradually disturbed, and directions of flow are generally pointed to outsides. The maximum velocity of the flow field can be observed near the tip of the cone. This is because when the cone penetrates through the soil, it imparts kinetic energy to the water, causing the water near the cone tip to flow. This also explains the drag force is concentrated around the penetrometer. The drag force associated with water flow velocity has the potential to move soil particles away from the cone, making the cone penetration process become more facilitated. The specific magnitude of facilitation is dependent on the magnitude of drag forces (see analysis above).

4.4 Discussion

From the above analysis, we can find that velocity affects penetration more significantly for saturated soils than dry soils (see Fig. 16a). For penetration in saturated soils, (1) soil penetration resistance decreases as the penetration rate increases; (2) normal contact force decreases with increasing penetration rate; (3) as the penetration velocity increases, the drag force generated near the cone tip becomes greater. These findings align with the experimental results carried out by Kim et al. [37]. To explain this phenomenon, Fig. 16b displays the fluid force variation with different penetration velocity. The drag force shows a significant increase with increasing velocity, whereas the pressure gradient force remains relatively constant, highlighting the greater sensitivity of drag force to changes in velocity compared to pressure gradient force. As the cone passes through the soil at a higher velocity, it provides a greater kinetic potential energy to the water, resulting in a rapid flow of water. This rapid fluid movement significantly increases the drag force of the fluid on the soil particles, and the resulting changes in the position and structure of the soil particles cause the soil particles in the area to become loose (less resistance). In contrast, penetration velocity has little effect on dry soils.

5 Conclusion

In this study, we simulate the CPT in saturated and dry soils with different penetration velocities by using a CFD–DEM coupled method. The influence of penetration rate and pore water was analyzed from both macro and micro perspectives. Some key conclusions can be drawn as follows.

(1) From macroscopic perspective, increasing the penetration velocity reduces the resistance of saturated soil, whereas the dry sample is barely affected.

(2) The displacement and velocity field of soil particles vary similarly for different velocities, for both dry and saturated cases. The area surrounding the cone penetrometer demonstrates the most significant soil particle movement and the greatest velocity field. For saturated soils, the normal contact force decreases with increasing penetration velocity; however, the effect on dry soils can be ignored in comparison to saturated soils.

(3) As the penetration rate increases, soil penetration resistance and normal contact force both decreases, while the drag force generated near the cone tip significantly increases. Increase in drag force rather than pressure gradient force leads to facilitation of
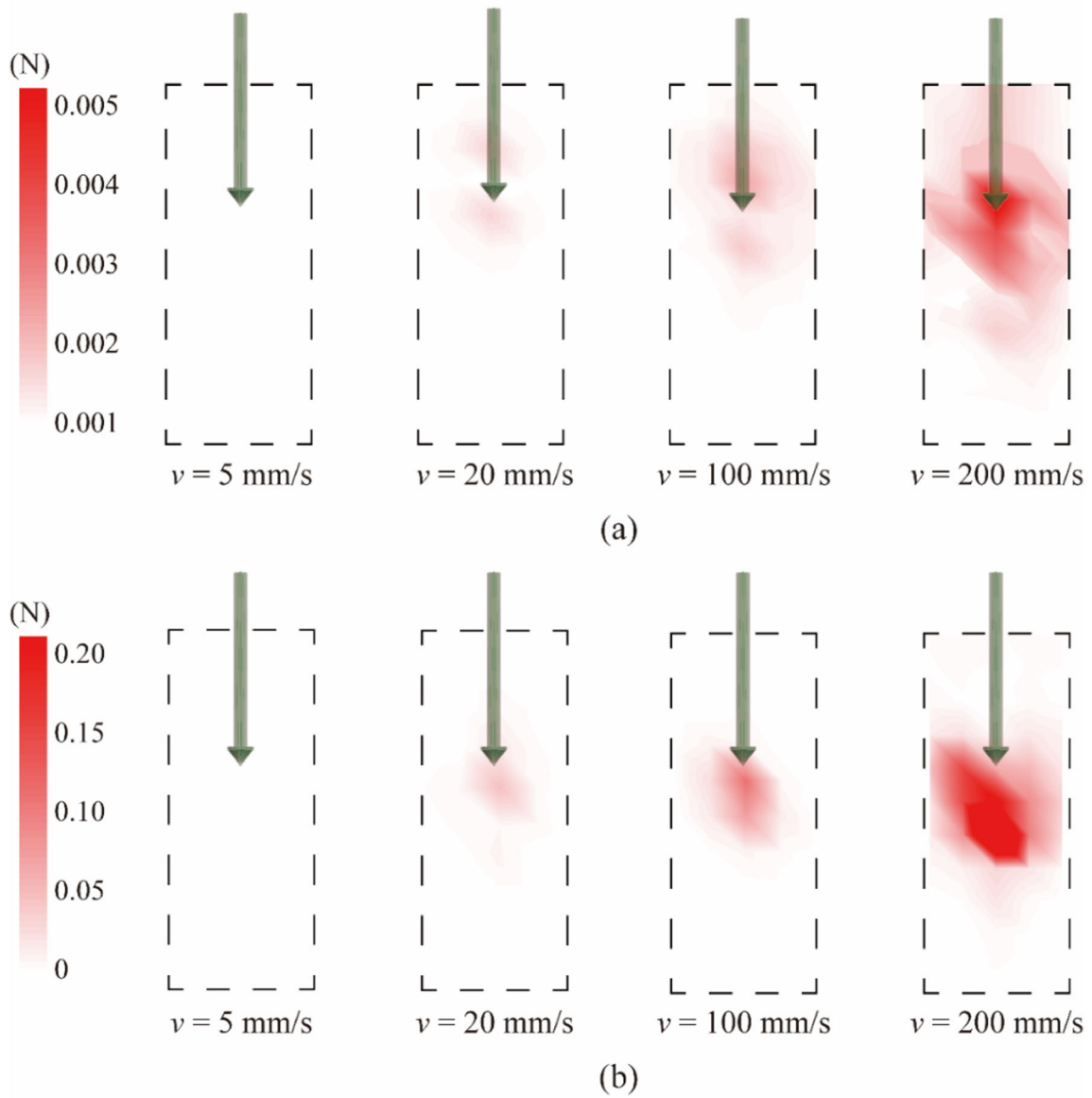
Fig. 13 Evolution of fluid force at different penetration velocities. **a** Pressure gradient force; **b** drag force
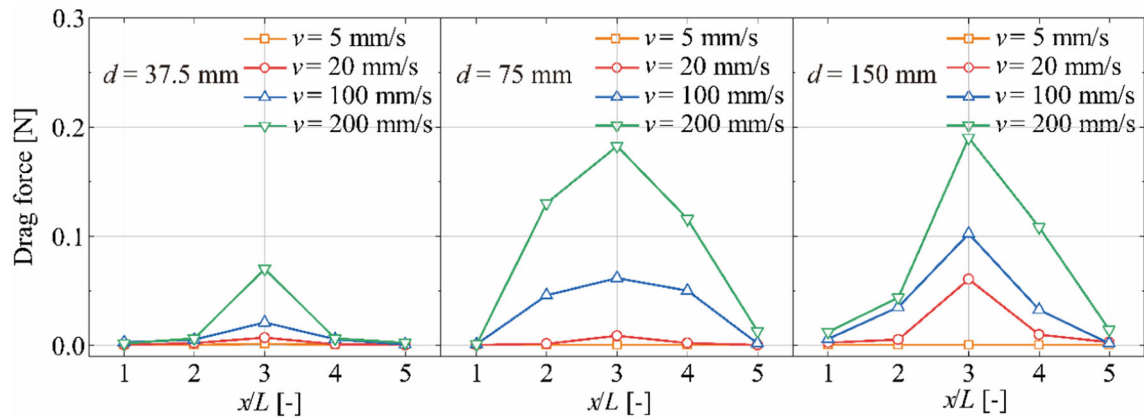

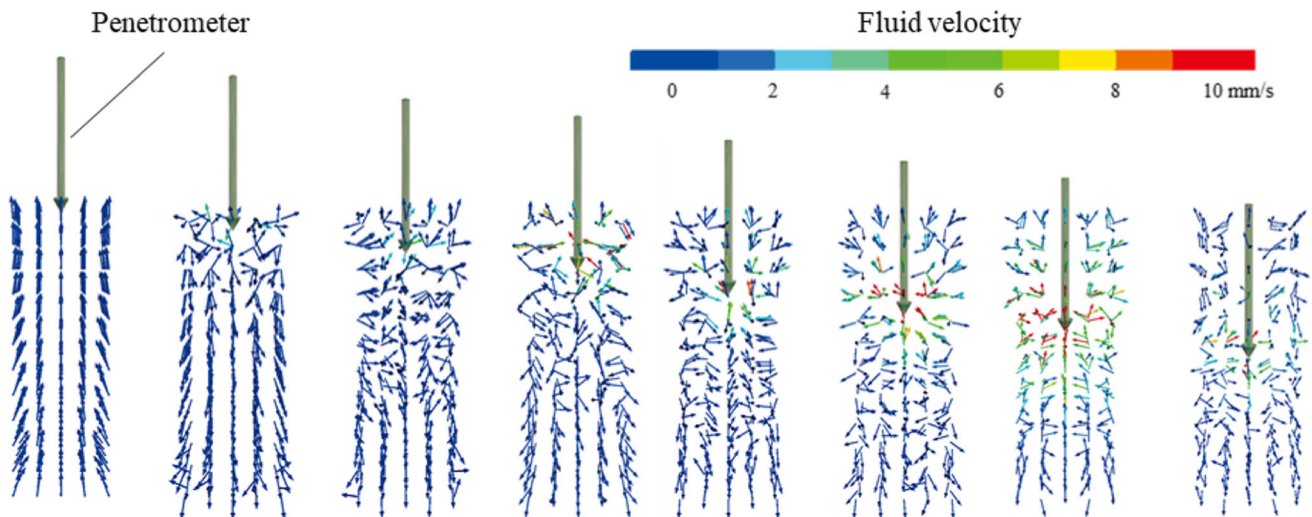Fig. 14 The drag force distribution on the x-axis with depth under various penetration velocities

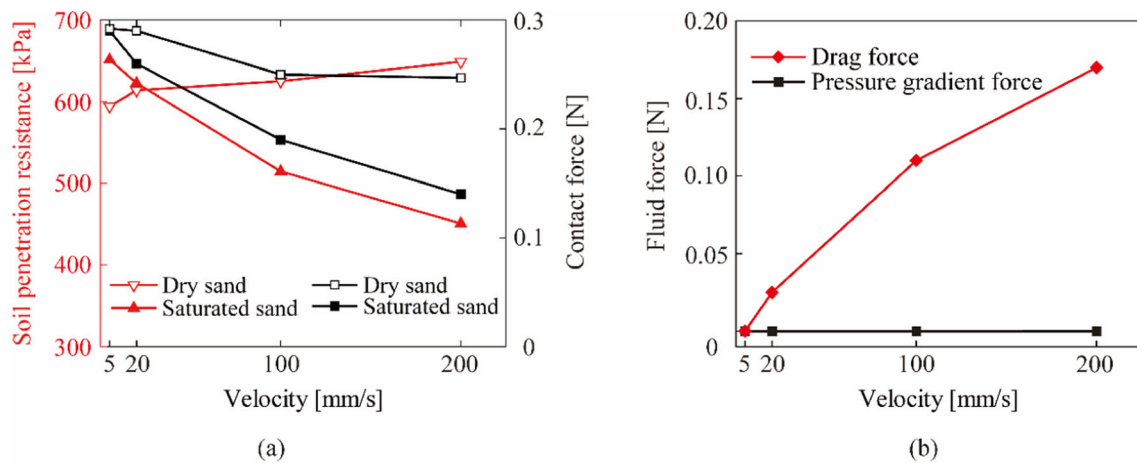**Fig. 15** Evolution of fluid velocity at a penetration rate of 20 mm/s

Fig. 16 The force characteristics of soil particles under different penetration velocities. **a** Penetration resistance and contact force; **b** fluid force

penetration in saturated soils with high penetration rate. However, the penetration rate had little effect on the cone tip resistance of the dry soil.

6 Limitations

In this study, the proposed model focuses more on the rapid drainage soil using CFD and DEM, which has some disadvantages on simulation of poor drainage soil, such as clayey soils, due to high computational requirements. Future research may focus on addressing these limitations through the development of more efficient computational algorithms for soil water interactive systems.

Author contributions GY contributed to conceptualization, methodology, data curation, investigation, writing—original draft. AZ contributed to conceptualization, methodology, investigation, supervision, funding acquisition, writing—original draft. MN contributed to investigation, supervision, funding acquisition, writing—review & editing. YD contributed to investigation, writing—review & editing.

Declarations

References

1. Abu-Farsakh MY, Voyiadjis GZ, Tumay MT (1998) Numerical analysis of the miniature piezocone penetration tests (PCPT) in cohesive soils. Int J Numer Anal Meth Geomech 22(10):791–818

2. Akhshik S, Behzad M, Rajabi M (2016) CFD–DEM simulation of the hole cleaning process in a deviated well drilling: the effects of particle shape. Particuology 25:72–82

3. Allulakshmi K, Vinod JS, Heitor A, Fourie A (2022) Numerical modeling of cone penetration test: an LBM–DEM approach. Int J Geomech 22(8):04022125

4. Anderson TB, Jackson R (1967) Fluid mechanical description of fluidized beds. Equations of motion. Ind Eng Chem Fundam 6(4):527–539

5. Aubram D, Rackwitz F, Wriggers P, Savidis SA (2015) An ALE method for penetration into sand utilizing optimization-based mesh motion. Comput Geotech 65:241–249

6. Berezantzev V (1961) Load bearing capacity and deformation of piled foundations. In: Proc. of the 5th international conference, ISSMFE, Parisn. pp 11–12

7. Beuth L, Vermeer P (2013) Large deformation analysis of cone penetration testing in undrained clay. Installation effects in geotechnical engineering. Taylor & Francis Group, London

8. Biarez J, Burel M, Wack B (1961) Contribution à l'étude de la force portante des fondations. In: Proc., V Intl. Conf. Soil Mech. Found. Eng., Paris, France. vol 603. p 6

9. Bisht V, Salgado R, Prezzi M (2021) Material point method for cone penetration in clays. J Geotech Geoenviron Eng 147(12):04021158

10. Bojanowski C (2014) Numerical modeling of large deformations in soil structure interaction problems using FE, EFG, SPH, and MM-ALE formulations. Arch Appl Mech 84(5):743–755

11. Bolton M, Gui M (1993) The study of relative density and boundary effects for cone penetration tests in centrifuge. University of Cambridge, Department of Engineering

12. Butlanska J, Arroyo M, Gens A, O'Sullivan C (2014) Multi-scale analysis of cone penetration test (CPT) in a virtual calibration chamber. Can Geotech J 51(1):51–66

13. Butlanska J, O'Sullivan C, Arroyo M, Gens A, Jiang M, Liu F, Bolton M (2011) Mapping deformation during CPT in a virtual calibration chamber. In: Proceedings of the international symposium on geomechanics and geotechnics: from micro to macro. Taylor & Francis Group. pp 559–564

14. Ceccato F, Beuth L, Simonini P (2016) Analysis of piezocone penetration under different drainage conditions with the two-phase material point method. J Geotech Geoenviron Eng 142(12):04016066

15. Ceccato F, Beuth L, Vermeer P, Simonini P (2015) Two-phase material point method applied to cone penetration for different drainage conditions. In: Geomech. from Micro to Macro-Proc. TC105 ISSMGE Int. Symp. Geomech. from Micro to Macro, Cambridge. pp 965–970

16. Ceccato F, Beuth L, Vermeer PA, Simonini P (2016) Two-phase material point method applied to the study of cone penetration. Comput Geotech 80:440–452

17. Ciantia MO, Arroyo M, Butlanska J, Gens A (2016) DEM modelling of cone penetration tests in a double-porosity crushable granular material. Comput Geotech 73:109–127

18. Cundall PA, Strack O (1979) A discrete numerical model for granual assemblies. Geotechnique 29(1):47–65

19. Di Felice R (1994) The voidage function for fluid-particle interaction systems. Int J Multiph Flow 20(1):153–159

20. Drew DA (1983) Mathematical modeling of two-phase flow. Annu Rev Fluid Mech 15(1):261–291

21. Durgunoglu HT, Mitchell JK (1973) Static penetration resistance of soils. No. SSL-SER-14-ISSUE-24

22. Ergun S (1952) Fluid flow through packed columns. Chem Eng Prog 48:89–94

23. Falagush O, McDowell G, Yu H-S (2015) Discrete element modeling of cone penetration tests incorporating particle shape and crushing. Int J Geomech 15(6):04015003

24. Falagush O, McDowell GR, Yu H-S, de Bono JP (2015) Discrete element modelling and cavity expansion analysis of cone penetration testing. Granular Matter 17(4):483–495

25. Foster WA Jr, Johnson CE, Chiroux RC, Way TR (2005) Finite element simulation of cone penetration. Appl Math Comput 162(2):735–749

26. Gupta RC (1991) Finite strain analysis for deep cone penetration. J Geotech Eng 117(10):1610–1630

27. House A, Oliveira J, Randolph M (2001) Evaluating the coefficient of consolidation using penetration tests. Int J Phys Model Geotech 1(3):17–26

28. Hu G (1965) Bearing capacity of foundations with overburden shear. Sols-Soils 13:11–18

29. Huang A-B, Ma MY (1994) An analytical study of cone penetration tests in granular material. Can Geotech J 31(1):91–103

30. Huang W, Sheng D, Sloan S, Yu H (2004) Finite element analysis of cone penetration in cohesionless soil. Comput Geotech 31(7):517–528

31. Jäger R, Mendoza M, Herrmann HJ (2018) Clogging at pore scale and pressure-induced erosion. Phys Rev Fluids 3(7):074302

32. Jezequel J (1969) Les Pénétromètres Statiques. Influence Du Mode D'emploi Sur La Résistance de Pointe. Bidl de Liaison de Laboratoire Routiers de Ponts de Chaussees 36:151–160

33. Jiang M, Yu HS, Harris D (2006) Discrete element modelling of deep penetration in granular soils. Int J Numer Anal Meth Geomech 30(4):335–361

34. Juran I, Tumay MT (1989) Soil stratification using the dual pore-pressure piezocone test. Transp Res Rec 1235:68–78

35. Khodayari M, Ahmadi M (2020) Excess pore water pressure along the friction sleeve of a piezocone penetrating in clay: Numerical study. Int J Geomech 20(7):04020100

36. Khosravi A, Martinez A, DeJong J (2020) Discrete element model (DEM) simulations of cone penetration test (CPT) measurements and soil classification. Can Geotech J 57(9):1369–1387

37. Kim K, Prezzi M, Salgado R, Lee W (2008) Effect of penetration rate on cone penetration resistance in saturated clayey soils. J Geotech Geoenviron Eng 134(8):1142–1153

38. Kinloch H, O'Sullivan C (2007) A micro-mechanical study of the influence of penetrometer geometry on failure mechanisms in granular soils. In: Advances in Measurement and Modeling of Soil Behavior. pp 1–11

39. Kiousis PD, Voyiadjis GZ, Tumay MT (1988) A large strain theory and its application in the analysis of the cone penetration mechanism. Int J Numer Anal Meth Geomech 12(1):45–60

40. Kotrocz K, Mouazen AM, Kerényi G (2016) Numerical simulation of soil–cone penetrometer interaction using discrete element method. Comput Electron Agric 125:63–73

41. Lehane B, O'loughlin C, Gaudin C, Randolph M (2009) Rate effects on penetrometer resistance in kaolin. Géotechnique 59(1):41–52

42. Liu Y, Wang L, Hong Y, Zhao J, Yin ZY (2020) A coupled CFD-DEM investigation of suffusion of gap graded soil: coupling effect of confining pressure and fines content. Int J Numer Anal Meth Geomech 44(18):2473–2500

43. Lunne T, Powell JJ, Robertson PK (2002) Cone penetration testing in geotechnical practice. CRC Press, Boca Raton

44. Máthé L, Kiss P, Laib L, Pillinger G (2013) Computation of run-off-road vehicle speed from terrain tracks in forensic investigations. J Terrramech 50(1):17–27

45. Moug DM, Boulanger RW, DeJong JT, Jaeger RA (2019) Axisymmetric simulations of cone penetration in saturated clay. J Geotech Geoenviron Eng. https://doi.org/10.1061/(ASCE)GT.1943-5606.0002024

46. Nazem M, Carter JP, Airey DW, Chow S (2012) Dynamic analysis of a smooth penetrometer free-falling into uniform clay. Géotechnique 62(10):893–905

47. Oliveira JR, Almeida MS, Motta HP, Almeida MC (2011) Influence of penetration rate on penetrometer resistance. J Geotech Geoenviron Eng 137(7):695–703

48. Parkin A, Lunne T (1982) Boundary effects in the laboratory calibration of a cone penetrometer for sand. Norwegian Geotechnical Institute Publication, Oslo

49. Potyondy DO, Cundall P (2004) A bonded-particle model for rock. Int J Rock Mech Min Sci 41(8):1329–1364

50. Presti DL, Squeglia N, Meisina C, Visconti L (2010) Use of CPT and CPTu for soil profiling of "intermediate" soils: a new approach. pp 1–8

51. Qian J-G, Zhou C, Yin Z-Y, Li W-Y (2021) Investigating the effect of particle angularity on suffusion of gap-graded soil using coupled CFD–DEM. Comput Geotech 139:104383

52. Randolph M, Hope S (2004) Effect of cone velocity on cone resistance and excess pore pressures. Effect of cone velocity on cone resistance and excess pore pressures. Yodogawa Kogisha Co. Ltd, Osaka, pp 147–152

53. Sacchetto M, Trevisan A (2010) Influence of rate of penetration on CPT tip resistance in standard CPT and in CPTWD (CPT while drilling). In: Proceedings of 2nd international symposium on cone penetration testing, CPT

54. Salgado R, Mitchell J, Jamiolkowski M (1997) Cavity expansion and penetration resistance in sand. J Geotech Geoenviron Eng 123(4):344–354

55. Schneider JA, Lehane BM, Schnaid F (2007) Velocity effects on piezocone measurements in normally and over consolidated clays. Int J Phys Model Geotech 7(2):23–34

56. Sharif YU, Brown MJ, Ciantia MO, Cerfontaine B, Davidson C, Knappett J, Meijer GJ, Ball J (2021) Using discrete element method (DEM) to create a cone penetration test (CPT)-based method to estimate the installation requirements of rotary-installed piles in sand. Can Geotech J 58(7):919–935

57. Susila E, Hryciw RD (2003) Large displacement FEM modelling of the cone penetration test (CPT) in normally consolidated sand. Int J Numer Anal Methods Geomech 27:586–602

58. Suzuki K, Bardet JP, Oda M, Iwashita K, Tsuji Y, Tanaka T, Kawaguchi T (2007) Simulation of upward seepage flow in a single column of spheres using discrete-element method with fluid-particle interaction. J Geotech Geoenviron Eng 133(1):104–109

59. Suzuki Y (2015) Investigation and interpretation of cone penetration rate effects. University of Western Australia Crawley, Australia

60. Suzuki Y, Lehane B (2015) Analysis of CPT end resistance at variable penetration rates using the spherical cavity expansion method in normally consolidated soils. Comput Geotech 69:141–152

61. Takesue K, Sasao H, Makihara Y (1996) Cone penetration testing in volcanic soil deposits. In: Advances in site investigation practice. Proceedings of the International Conference held in London on 30–31 March 1995

62. Tanaka H, Momozu M, Oida A, Yamazaki M (2000) Simulation of soil deformation and resistance at bar penetration by the distinct element method. J Terrramech 37(1):41–56

63. Terzaghi K (1943) Theoretical soil mechanics. John Wiley and Sons Inc., New York, p 314

64. Tsuji Y, Kawaguchi T, Tanaka T (1993) Discrete particle simulation of two-dimensional fluidized bed. Powder Technol 77(1):79–87

65. Vesic AB (1963) Bearing capacity of deep foundations in sand. Highway Research Record

66. Vesic AS (1972) Expansion of cavities in infinite soil mass. J Soil Mech Found Div 98:265–290

67. Wang D, Bienen B, Nazem M, Tian Y, Zheng J, Pucker T, Randolph MF (2015) Large deformation finite element analyses in geotechnical engineering. Comput Geotech 65:104–114

68. Xiong H, Yin Z-Y, Zhao J, Yang Y (2021) Investigating the effect of flow direction on suffusion and its impacts on gap-graded granular soils. Acta Geotech 16(2):399–419

69. Xu B, Yu A (1997) Numerical simulation of the gas-solid flow in a fluidized bed by combining discrete particle method with computational fluid dynamics. Chem Eng Sci 52(16):2785–2809

70. Yi J, Goh S, Lee F, Randolph M (2012) A numerical study of cone penetration in fine-grained soils allowing for consolidation effects. Géotechnique 62(8):707–719

71. Yu H-S (2000) Cavity expansion methods in geomechanics. Springer Science & Business Media, Dordrecht

72. Yu H, Herrmann L, Boulanger R (2000) Analysis of steady cone penetration in clay. J Geotech Geoenviron Eng 126(7):594–605

73. Yu H, Houlsby G (1991) Finite cavity expansion in dilatant soils: loading analysis. Géotechnique 41(2):173–183

74. Zhao J, Shan T (2013) Coupled CFD–DEM simulation of fluid–particle interaction in geomechanics. Powder Technol 239:248–258